ADVANCED SCIENCE NEWS
www.advancedsciencenews.com

Hierarchical Branched Vanadium Oxide Nanorod@ Si Nanowire Architecture for High Performance Supercapacitors

*Zhaodong Li, Fei Wang, and Xudong Wang**

As one of the most promising strategies for next generation energy storage, electrochemical supercapacitor has received considerable attention worldwide owing to its high-power density, fast charging/discharging, excellent cycling stability, and low maintenance.[1–4] Electrochemical double-layer capacitors (EDLCs) are one major type of supercapacitor design that stores electrical energy by accumulating ions on electrode surface resulting in the high energy density and high-rate capability.[5] Pseudocapacitor, on the other hand, makes use of fast redox reactions or phase changes at the surface or subsurface of active materials with the potential to achieve higher energy density than EDLCs.[6,7] Generally, high-capacitance electrode requires a high surface area and good electrical conductivity. These features are strongly related to the electrochemical double layer capacitance and/or electrochemical activity of electrode surfaces.[2,5,8] Therefore, one major strategy to improve the performance of supercapacitors is to construct complex nanostructured electrodes with hierarchical structure, adequate charge transport properties, as well as suitable thickness and surface chemical properties.

3D hierarchical nanostructures have been increasingly studied in electrochemical applications due to their extremely large surface-to-volume ratio, excellent permeability, and high-density surface active sites.[3,9–14] Owing to the extraordinary capability of conformal and pinhole-free coating capability, atomic layer deposition (ALD) was often used for directly depositing active materials on 3D nanostructured templates for supercapacitor electrode fabrication.[15–17] The high-quality ALD films are essential for controlling ion intercalation and diffusion into the bulk electrodes to achieve high capacity.[8,18] Meanwhile, the 3D nanotemplates need to be conductive for rapid and low-loss charge transport. In order to integrate all the desired features in one coherent heterostructure, an emerging promising concept is to directly synthesize nanostructure arrays from pseudocapacitive materials on conductive nanotemplates as binder-free electrodes. The surface-reaction-limited pulsed chemical vapor deposition (SPCVD) technique developed in our lab has the unique capability of growing uniform TiO_2 nanorod (NR) branches on dense and deep Si nanowire (NW) arrays, offering a novel hierarchical 3D NW architecture with enhanced electrical and electrochemical properties.[13] Further understanding of the growth kinetics[19] suggested this technique could be broadly applied to other functional materials, such as vanadium oxide (VO_x) NR branches for supercapacitor applications. This configuration could simultaneously achieve high surface area, multiple accessible electroactive sites, short ion transport pathways, and superior electron collection efficiency, which are essential to delivering high specific capacitance, sustained cycle life, and rate performance. Driven by this hypothesis, in this work, pseudocapacitive VO_x NRs branches were synthesized on Si NW backbones creating a unique 3D hierarchical VO_x NRs@Si NWs structure. The superior electrochemical performance of the structure was demonstrated. In addition, the calcination atmosphere could tune the chemical compositions of VO_x NRs and manipulate their supercapacitor performance. This development presents a new 3D nanomaterial platform for high-performance supercapacitor electrodes design.

Figure 1a,b presents a typical morphology of as-synthesized VO_x NRs@Si NWs hierarchical structure by scanning electron microscopy (SEM). Dense VO_x NRs branched from Si NW bundles and protruded outward radially (Figure 1a). Higher magnification image reveals that the dimensions of the NR branches were ≈250 nm in length and ≈30 nm in diameter (inset of Figure 1a). The VO_x NRs were uniformly distributed along the entire side surfaces of the Si NWs that were 3 μm in length and only ≈100–200 nm apart from each other (Figure 1b). The VO_x NRs exhibited a rectangular prism shape and were all rooted on the Si surfaces (inset of Figure 1b). Such an NR 3D architecture offered a superiority on surface areas, where the roughness factor reached 140 (cal.). This number is nearly ten times higher than pure NW arrays with the same vertical length. After annealing at 500 °C in H_2 or O_2 atmosphere, the morphology and hierarchical structure of VO_x NRs were well preserved (Figure S1a,b, Supporting Information, respectively), suggesting the VO_x NRs had good thermal stability. In addition, the contrast variation in these images under a constant SEM brightness indicates the possible resistivity difference of the samples, which may come from the change

Z. Li, Dr. F. Wang, Prof. X. D. Wang
Department of Materials Science and Engineering
University of Wisconsin-Madison
Madison, WI 53706, USA
E-mail: xudong@engr.wisc.edu

DOI: 10.1002/smll.201603076

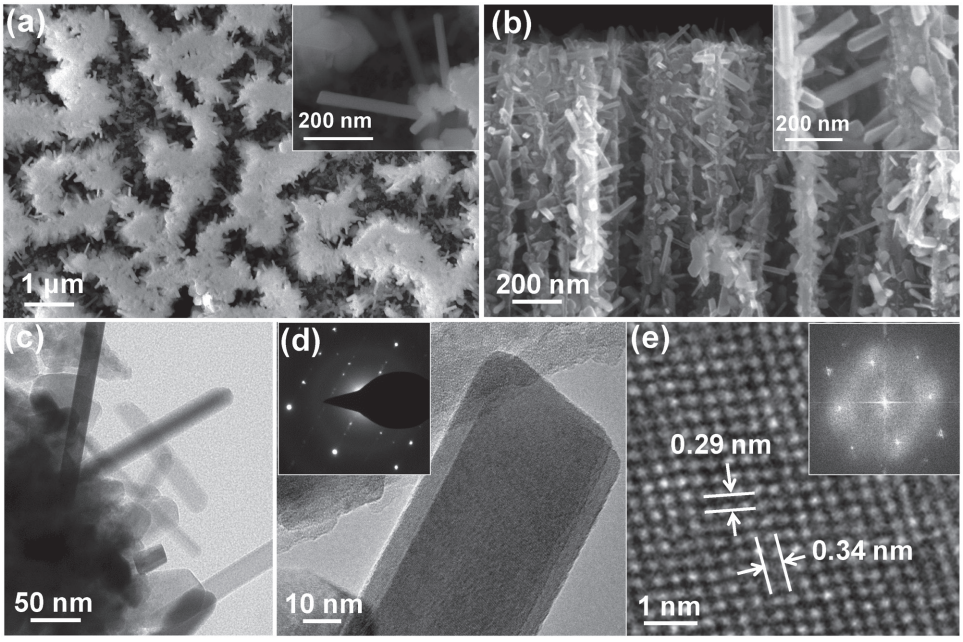

Figure 1. SEM of typical morphologies of as-synthesized VO_x NRs@Si NWs hierarchical structures. a) Top view and b) cross section view; insets indicating the dimensions of the NR branches were ≈250 nm in length and ≈30 nm in diameter. c,d) TEM images of typical morphologies and crystal structures of as-synthesized VO_x NRs@Si NWs hierarchical structures. c) Si backbone is uniformly covered by ultrathin NRs. d) HRTEM image shows the rectangular shape of the NR with a flat tip surface. Inset SAED pattern confirmed single crystallinity of the V_2O_5 phase, and e) the lattice fringes were indexed as the (301) and (110) planes of V_2O_5, respectively.

of vanadium-based oxides phases by the modification of the calcination atmosphere.[20]

Transmission electron microscopy (TEM) was used to further study the morphology and crystal structure of the VO_x NRs. Figure 1c shows a TEM image of VO_x NRs rooted on Si NW surface. The surfaces of Si backbone were uniformly covered by ultrathin NRs. Closer observation shows the rectangular shape of the NR with a flat tip surface (Figure 1d). Corresponding selected area diffraction (SAED) pattern (inset of Figure 1d) confirmed single crystallinity of the vanadium pentoxide (V_2O_5) phase. From the high-resolution TEM (HRTEM) image shown in Figure 1e, the lattice fringes were identified with an interplanar spacing of 0.29 and 0.34 nm, which were indexed as the (301) and (110) planes of V_2O_5, respectively. Notably, a few NRs exhibited a sword-like tip whereas their diameter was nearly identical to the flat-tip NRs. These NRs were found to be the VO_2 phase. The lattice spacing was determined to be 0.23, 0.25, and 0.25 nm from the fast fourier transform (FFT)of the HRTEM image (Figure S2, Supporting Information), matching well to the (020), $(2\bar{1}\bar{1})$, and $(21\bar{1})$ planes of VO_2, respectively. Therefore, the as-synthesized VO_x NRs contained both V_2O_5 and VO_2 phases. Figure S3a,b (Supporting Information) shows a VO_x NR after annealing in H_2 atmosphere. The NR surfaces were covered by a ≈3–4 nm thick percolated layer, a mixture of randomly oriented nanocrystals with amorphous intercalations. This is different from the sharp edges that were observed from the as-prepared VO_x NRs (Figure 1d). Formation of the percolated layer revealed the significant vanadium-based oxide phase transition at the surface during hydrogen treatment. In comparison, the VO_x NR after O_2 annealing held much better crystal quality despite some lattice distortions occurred at the NR's surface (Figure S3c,d, Supporting Information).

X-ray diffraction (XRD) was used to further analyze the mixed phase and phase evolution of VO_x NRs upon different heat treatments (Figure S4, Supporting Information). Both V_2O_5 and VO_2 exhibited significant signal in the as-received VO_x NR@Si sample, which is consistent with the TEM observation. After H_2 treatment, the VO_2 phase became more dominant in the sample due to the partial reduction of vanadium oxide. The mixed-valent VO_x has been found beneficial for the electrochemical pseudocapacitor application.[2,20] When the sample was annealed in O_2 atmosphere, however, the vanadium oxide phase in the NR was completely converted into V_2O_5. It was also found that the pure V_2O_5 was obtained from ALD VO_x films grown at 350 °C. The temperature-related phase variation was consistent with others' work where different valance states of vanadium were obtained by chemical vapor deposition at different temperature using the same precursors ($VOCl_3$ and H_2O).[21,22]

The surface chemistry and elemental information of VO_x NRs and films are an essential factor for the supercapacitor performance, and they were studied by X-ray photoelectron spectroscopy (XPS). **Figure 2**a shows the full spectra of XPS survey scans from the VO_x films, as-received, H-treated and O-treated VO_x NRs, in which elements of Si, V, and O can be clearly identified. To analyze the surface chemical states, the V 2p region near 520 eV of the XPS spectra were examined (Figure 2b). All samples exhibited a typical two-peak structure (V $2p_{3/2}$ and V $2p_{1/2}$) due to the spin–orbit splitting. Broader V $2p_{3/2}$ and V $2p_{1/2}$ peaks were observed in as-synthesized VO_x NRs and H_2 treated VO_x NRs compared to those from O_2 treated VO_x NRs and VO_x

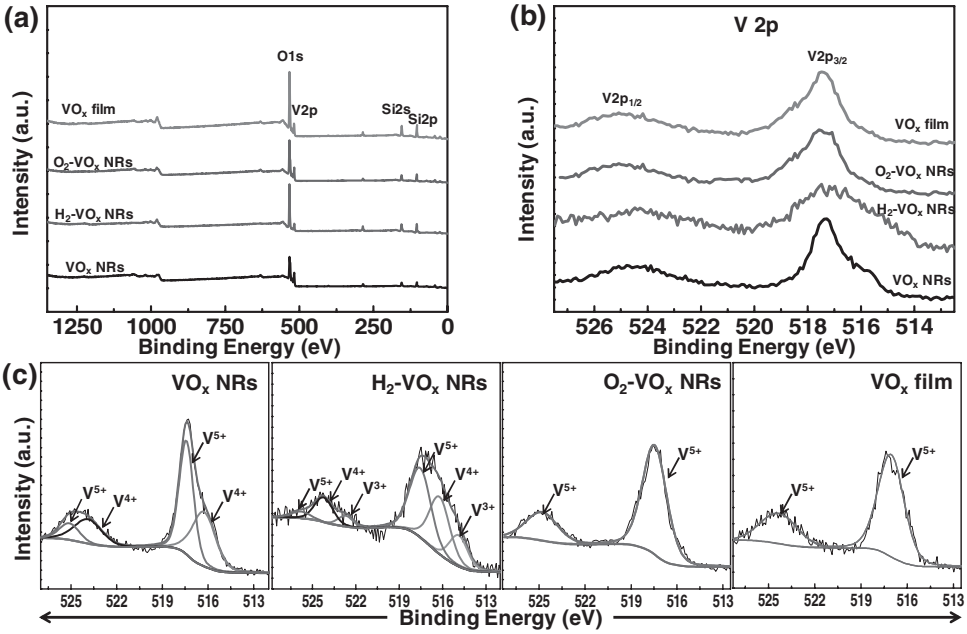

Figure 2. XPS characterization of VO_x NRs and films. a) Full XPS spectra. b) V 2p scan near 520 eV. c) The deconvoluted spectra for V 2p peak of all samples upon different prepare conditions. The mixed valence states were found in as-synthesized NRs. H_2 treatment introduced more mixed valence states, whereas O_2 treatment converted it into pure V_2O_5 phase. The same pure V_2O_5 phase was observed on ALD VO_x film sample.

films. In order to elucidate the different chemical binding states of the V element, the deconvoluted spectra for V 2p peaks were investigated (Figure 2c). The binding energies of V^{5+}, V^{4+}, and V^{3+} valence states to the V $2p_{3/2}$ peak could be assigned at 518.0, 516.4, and 514.8 eV, respectively. For the V $2p_{1/2}$ peak, such binding energies were assigned at 525.4, 524.1, and 522.4 eV, respectively.[20] The V^{5+} and V^{4+} states were observed in as-synthesized VO_x NRs, which was consistent with the TEM and XRD results. The valence states would be further reduced by extra H_2 treatment, and therefore, the V^{3+} states were discovered in H_2-VO_x NRs. However, V^{3+}-related structure was not observed from the XRD spectra, suggesting the amount of V^{3+} may not be significant enough to form as isolated phase and they might be contained in the percolated thin layer around the NRs. No lower chemical states of vanadium were observed from the oxygen-treated sample, further confirming that the VO_x NRs were fully transferred to the V_2O_5. The pure V_2O_5 phase was also obtained for the ALD vanadium oxide film sample.

The mixed valence states of metal oxide have been found being able to enable multiple charge storage mechanisms with small internal resistance, and highly reversible and faster charge transfer kinetics.[2] Typically, vanadium oxide was applied as a negative material of supercapacitor since the intercalate of Li^+ into VO_x leading the reduction of vanadium during the charging cycle.[23,24] Prior to applying the VO_x NRs@Si NWs architecture to supercapacitor system, an additional layer of VO_x polycrystalline thin film was deposited by ALD (typically 100 cycles) to completely cover the Si surfaces and prevent the contact between Si and electrolyte. When LiCl is utilized as the electrolyte, as shown in **Figure 3**a, such reversible redox transitions likely included the insertion/extraction of lithium ions as well as the transitions between different valence states of vanadium.[23–25] In addition, owing to the mixed compositions of vanadium oxide, excellent surface/body ratios, and the conductive Si NW cores, the 3D hierarchical VO_x NRs@Si NWs heterostructure could be a promising electrode structure for supercapacitor design. Cyclic voltammetry (CV) measurement was performed on as-synthesized VO_x NRs in an 8 M LiCl solution with a scan rate from 1 mV s^{-1} to 2 V s^{-1} (Figure 3b). The 1.2 V potential window (–0.5 to 0.7 V) is the maximum value of VO_x-based supercapacitors in LiCl electrolyte.[1,26] Although there was no distinct sharp redox peaks in the CV profile, the shape of the curve deviated from the ideal rectangle, implying its faradaic pseudocapacitive nature.[27] Such pseudocapacitance is usually considered to be originated from the charge transfer in surface redox reactions of VO_x. Meawhile, peaks were observed at –0.4 and 0.4 V on the anodic–cathodic curves, demonstrating the possible bulk redox reaction also occurred on VO_x NRs. This battery-behavior provided a substaintial amount of charge-storage capacity additional to pseudocapacitance.[28] Notably, the peaks were weak but broad, which indicates the charge exchange between the VO_x NRs and the LiCl electrolyte was almost independent of the applied bias. This characteristic was very similar to that of hydrous ruthenium oxide, which was a characteristic of ideal pseudocapacitor-like materials.[20,29] Moreover, the symmetric shape of the CV curves suggested that the VO_x NRs@Si electrode was highly reversible up to 2 V s^{-1}. This rate was higher than typically reported 0.1–1 V s^{-1} rates of oxide pseudocapacitors,[1,30,31] which indicates the impressive electrochemical stability of the SPCVD VO_x NRs during charge transfer. The current showed relatively sharp switches at the boundaries of the potential window, which could be attributed to the fast ion diffusion[32] and low electrode resistance[20] as a result of the

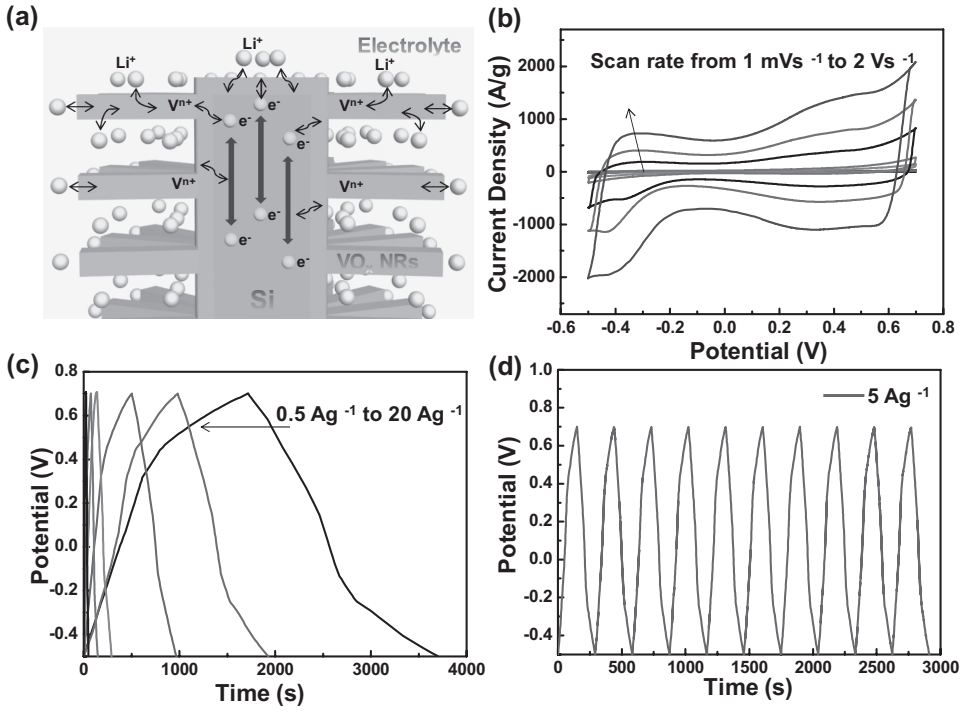

Figure 3. a) Schematic representation of electrochemical reaction mechanism by applying VO_x NRs@Si NWs hierarchical structures as supercapacitor electrode in LiCl. b) Cyclic voltammograms and c) charge–discharge profiles of as-synthesized VO_x NRs@Si electrodes. d) Repeated Charge–discharge behavior of as-synthesized VO_x NRs@Si supercapacitor electrodes, which exhibited good recyclability at high-current (≈5 A g^{-1}) charging/discharging processes.

branched hierarchical nanoarchitecture, the reduced vanadium valence states, and the conductive Si backbone.

The VO_x phase-related electrochemical performance was then studied on hydrogen- and oxygen-treated samples. CV curves of H_2-VO_x NRs were shown in Figure S5 (Supporting Information). The broad peak in the central region of the curve was typically related to battery-like Faradaic reactions.[31,33] Such reactions were proposed to be the manifestation of the intercalating process. This is possibly due to the existence of surface percolated layer of the VO_x, which could facilitate lithium ion intercalation into the VO_x NRs.[34] The H_2-VO_x NRs, therefore, exhibited a relatively poor stability in electrochemical reactions and a higher degree of deviation from a rectangular CV curve. However, the synergistic effect of VO_x and Si was likely introduced in the electrochemical reaction.[35] Thus, the larger potential window of 1.3 V was obtained compared to the as-synthesized VO_x NRs. When the VO_x NRs were converted to V_2O_5 NRs through oxygen annealing, the capacitance value significantly decreased as evidenced by the lower current density and narrower potential window (Figure S6, Supporting Information). This behavior could be explained by the contribution of high resistivity as well as the nearly perfect crystal phase of V_2O_5 NRs which resulted in decreased charge transport and sluggish lithium ion insertion kinetics. Nonetheless, the chemically stable V_2O_5 could be beneficial to the conservation of 3D hierarchical nanoarchitecture in electrochemical charging/discharging process.

In order to represent the conspicuous advantage of this 3D hierarchical VO_x nanoarchitecture for supercapacitor application, the ALD VO_x film was also deposited on Si NWs as a reference sample for CV measurement (Figure S7, Supporting Information). The same 1 V potential window was obtained due to its pure V_2O_5 component. However, the capacitance of ALD VO_x film was much lower, which was mainly because of the low conductivity of V_2O_5 film and the decreased surface area of the film geometry (Figure S8, Supporting Information). Meanwhile, the unsymmetrical curve indicated that the redox reaction was not very reversible, inferring the low chemical stability of the ALD VO_x film during charging/discharging processes.

Galvanostatic charge–discharge (C–D) was further conducted to reveal the specific capacitance of the supercapacitors at a constant current. The C–D profiles of each sample at different current densities from 0.5 to 20 A g^{-1} were shown in Figure 3c. The distorted linear shapes referred to the operation of pseudocapacitance for all samples, which further confirmed the faradaic pseudocapacitive appearance of the CV curves. It is noteworthy that a clear platform appeared when the charging process of H_2-VO_x NRs reached the positive potential boundary (Figure S5b, Supporting Information). Such a platform could be a result of ion intercalation and was usually observed in battery characterizations, which was consistent to the battery-like CV curves of H_2-VO_x NRs.[36–38] In generally, all electrodes exhibited good recyclability at high-current charging/discharging processes (Figure 3d).

The specific capacitance as a function of the scanning rate and current density was calculated from the CV curves. First, the area mass densities (σ) of the active materials were determined by the following equation

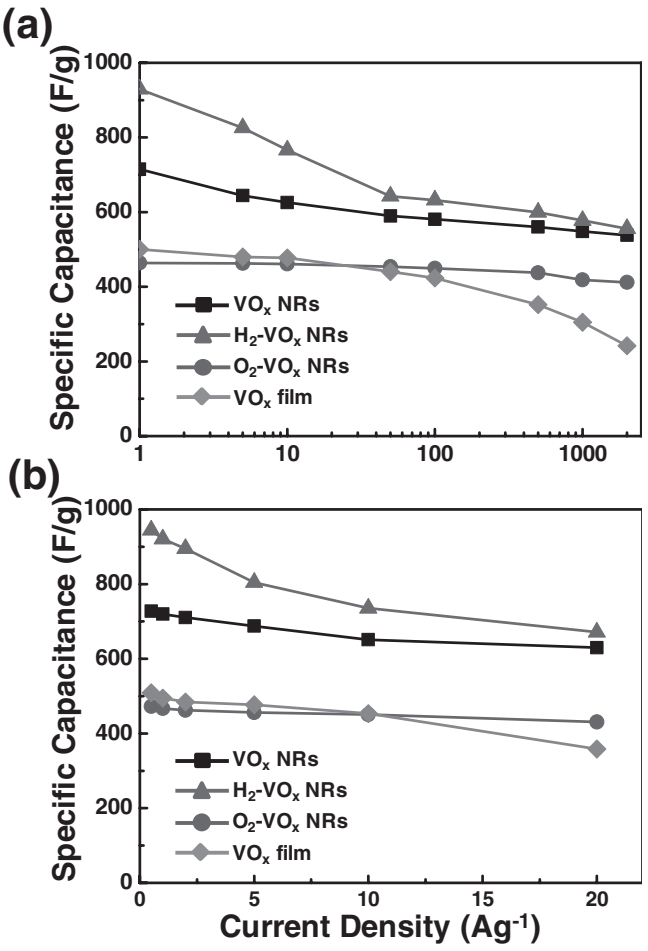

Figure 4. a) Specific capacitances calculated from the cyclic voltammetry curves measured with various scan rates. b) Specific capacitances calculated from galvanostatic charge/discharge with various current densities. H_2 and O_2 annealing were found to improve the specific capacitance and high-rate capability, respectively.

$$\sigma = (m_{\text{elec}} - m_{\text{SiNWs}})/A \quad (1)$$

where m_{elec} is the total mass of the electrode, $m_{\text{Si NWs}}$ is the mass of corresponding Si NWs substrate before the VO_x growth, and A is the area of the electrode. The active mass area density was calculated to be 1.35×10^{-6} g cm^{-2} (VO_x NRs@Si NWs), 1.12×10^{-6} g cm^{-2} (H_2-VO_x NRs@Si NWs), 1.65×10^{-6} g cm^{-2} (O_2-VO_x NRs@Si NWs), and 7.79×10^{-5} g cm^{-2} (VO_x films@Si NWs). Such extremely low mass shows the drastic advantage of this SPCVD technique owing to its development from ALD technique and has been widely used in energy-related areas.[39,40] By using Si nanostructured templates with lower mass but higher surface area, this technique could show unique merit in mass loading without influence the NRs growth.[19] In the three-electrode system, the specific capacitance based on the total mass of active material from CV data was calculated according to the equation

$$C = \frac{\Delta t}{2m\Delta V}\left(\int_{V^-}^{V^+} I(V)\,\mathrm{d}V - \int_{V^+}^{V^-} I(V)\,\mathrm{d}V\right) \quad (2)$$

where Δt is the discharging time; m is the total mass of active material which can be determined from the product of the area mass densities and active area of each electrode; ΔV is the potential window of discharge; V^- and V^+ are the negative and positive boundary values of the potential window, respectively; I is the discharge current. Since the vanadium pseudocapacitor exhibited an nonlinear galvanostatic C–D behavior, the specific capacitance was calculated by using the linear-fitting slope ($\Delta V/\Delta t$) of the discharge curve in whole charge–discharge windows.

As shown in **Figure 4**a, the as-received 3D hierarchical VO_x NRs@Si NWs electrode exhibited the highest specific capacitance of ≈710 F g^{-1} at the scan rate of 1 mV s^{-1}. Even at the ultrahigh sweeping rate of 2 V s^{-1}, the capacitance remains as high as ≈580 F g^{-1}, which was much higher than the reported values (≈450–530 F g^{-1}) of VO_x-based supercapacitor electrodes.[5,20,31,41] Hydrogen treatment further improved the specific capacitance over all scan rates. A specific capacitance of ≈930 F g^{-1} was achieved at 1 mV s^{-1} while the value decreased to ≈590 F g^{-1} at a scan rate of 2 V s^{-1}. However, the high-rate storage capability of the H_2-VO_x NRs electrode was suffered by its unstable structures as discussed above. The most stable high-rate storage capability was obtained from the oxygen-treated VO_x NRs, whereas the specific capacitance was much lower due to its resistive V_2O_5 component. The value was ≈490 F g^{-1} at 1 mV s^{-1} and remained at ≈450 F g^{-1} when the scan rate increased up to 2 V s^{-1}. Although the ALD VO_x film had the same V_2O_5 composition and lower exposed surface area compared to the O_2-VO_x NRs, the specific capacitance obtained at small scan rates was higher than that of O_2-VO_x NRs. It is known that the pseudocapacitance of oxides can approach a very high value at low scan rate (≈1 mV s^{-1}) or when the particle sizes were very small, because, under these two conditions, electrolyte ions and electrons can both penetrate to the entire volume of oxides.[20] The less condensed polycrystalline V_2O_5 film produced by ALD at 350 °C (Figure S8c, Supporting Information) would promote the penetration of ions and electrons into the metal oxide. When the scan rate was high, the specific capacitance of ALD film significantly decreased due to its low stability under faster redox reactions. Meanwhile, such electrochemical instability of ALD VO_x film also led to the wretched high-rate capability and capacity retention, which will be discussed below.

The specific capacitance as a function of the discharging current density was calculated from the C–D curves according to

$$C = \frac{I\Delta t}{m\Delta V} \quad (3)$$

As shown in Figure 4b, with increasing current densities, the specific capacitance of all four samples decreased gradually. This observation revealed an excellent high-rate capability of the as-synthesized VO_x NRs@Si NWs as high-performance supercapacitor electrodes. Meanwhile, H_2 and O_2 annealing would further improve its specific capacitance and high-rate capability, respectively. The long-term capacitance retentions of all electrodes were evaluated by C–D characterization for 10 000 cycles at a constant current density of 2 A g^{-1} (**Figure 5**a). The supercapacitor based on the as-synthesized VO_x NRs retained ≈81.3% of the initial capacitance after

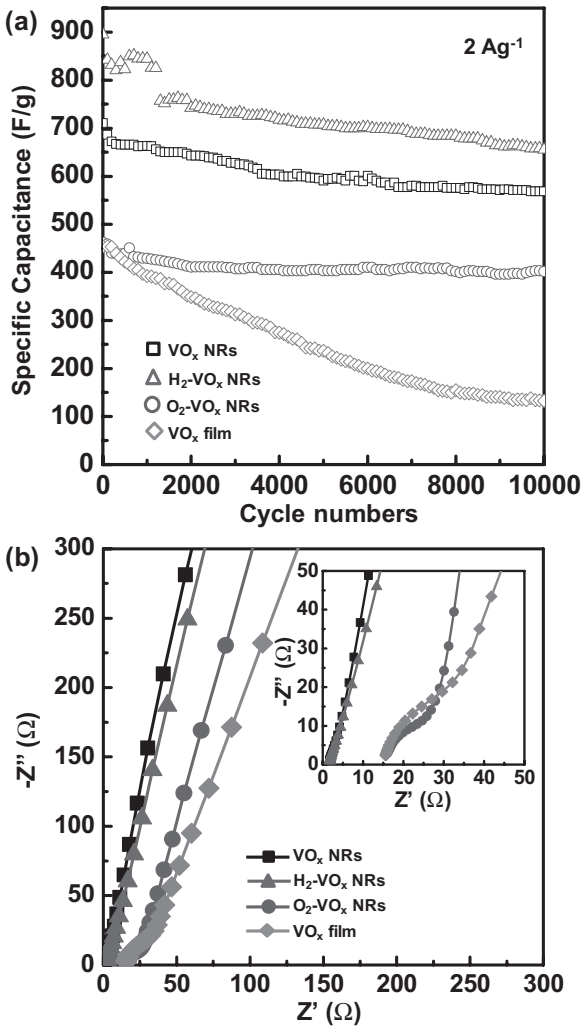

Figure 5. a) A typical specific capacitance values of different VO_x-Si electrodes as a function of charge–discharge cycle numbers. b) Nyquist plots of different VO_x-Si electrodes obtained over the frequency range of 100 kHz to 0.01 Hz by applying 10 mV alternative signal versus the open-circuit voltage; the smallest semicircle diameter indicates the lowest of resistance in all VO_x NRs@Si NWs electrode (inset is magnified figure at the high frequency).

10 000 cycles. The oxygen-treated sample showed the best stability with 91.1% capacity retained after the same number of charging/discharging cycles; while hydrogen-treated VO_x NRs had 70.3% capacity retained. The poorest stability was obtained from the VO_x films@Si NWs electrode, which only retained 31% of its original capacitance. Such retention variation was believed to be caused by the different chemical stability of the electrodes. The oxygen annealing created the most stable V_2O_5 phase, whereas the surface percolated layer introduced by H_2 treatment improved the specific capacitance but more quickly degraded during the electrochemical reaction. Overall, the high specific capacitance, excellent high-rate capability, as well as the capacitance retention of all 3D hierarchical VO_x NRs@Si NWs electrodes largely exceeded others' vanadium oxide-based electrodes (Table S1, Supporting Information).

Electrochemical impedance spectroscopy (EIS) was further performed to understand the electronic transport behavior of 3D hierarchical VO_x NRs@Si NWs structures. Nyquist plots derived from the EIS data were presented in Figure 5b with enlarged details shown in the inset. All four electrodes in this work showed typical features of supercapacitors. In the high-frequency region, the size of the semicircle implied the existence of charge-transfer resistance. As shown in the inset of Figure 5b, very small semicircles of both as-prepared and H_2 treated samples evidenced the rapid charge transport in these two electrodes. Besides, the charge-transfer resistances of all VO_x NRs samples in this work were found to be ranging from ≈6 to ≈16 Ω, which were comparable to the reported values (10–20 Ω) of vanadium oxide-carbon-based electrodes and much lower than those of stacked and bulk V_2O_5 electrodes (30–60 Ω).[1,5] The equivalent series resistance (ESR) was determined from the first interception on the real axis of the Nyquist curve, which represents the total resistance of electrolyte, electrodes, and the contact between the electrode and current collectors.[20,23,24] Small ESR was found from the as-synthesized and hydrogen-treated electrodes due to their better charge transport behavior. In addition, the increased slope of the line in the low-frequency region suggested an increased capacitive behavior for the as-synthesized and H_2 treated VO_x NRs.[42,43]

From the galvanostatic C–D results, the energy density (E) and power density (P) of each 3D hierarchical VO_x NRs@Si NWs structures were evaluated. The energy and power densities were calculated from the charge/discharge curves by the equations

$$E = \frac{C(\Delta V)^2}{2} \tag{4}$$

$$P = \frac{E}{t} \tag{5}$$

where E is the average energy density, C is the specific capacitance, ΔV is the discharge potential window, P is the average power density, and t is the discharge time. Strikingly, the as-synthesized 3D VO_x NRs@Si NWs structure exhibited a very high energy density of 145.5 Wh kg^{-1} at a power density of 264.1 W kg^{-1} and 126.0 Wh kg^{-1} at a power density of 11.4 kW kg^{-1}. Both energy density and power density were slightly higher for H_2-treated samples. Although the energy densities were significantly decreased from O_2-VO_x NRs@Si NWs electrodes, these values were still higher than the values of previously reported vanadium oxide-based electrode by applying the same electrolyte.[1,44,45]

In summary, we successfully synthesized high-density 3D hierarchical VO_x NRs@Si NWs structure for supercapacitor electrode development. The NW architecture could offer large surface areas, good charge transport properties, and mix-valance vanadium compositions. A 720 F g^{-1} specific capacitance was achieved from this 3D NW architecture at a discharging current density of 0.5 A g^{-1}, which was 38.5% higher than that of VO_x films@Si NWs structure. The comparison evidenced that a 3D NW architecture was superior to straight NW arrays for supercapacitor electrode design. Moreover, calcination of VO_x NRs in different atmospheres

was able to engineer the valence state and phase of VO_x NRs, and thus tuned their supercapacitor performance. The specific capacitance could be further improved by introducing more mix-valence vanadium compositions through H_2 annealing, with the maximum value approached 950 F g^{-1} at 0.5 A g^{-1}. O_2 annealing was able to convert all NRs to the pure V_2O_5 phase, which exhibited lower specific capacitances but enhanced high-rate capability and stability. The as-synthesized VO_x NRs had good cyclability with ≈81.3% of the initial capacitance retained after 10 000 cycles. Both energy density and power density were significantly improved by the 3D NW architectures compared to other reported regular geometries. This facile and low-cost technique introduced a novel route toward high-performance supercapacitor electrodes design using high-density 3D hierarchical NWs.

Experimental Section

Preparation of 3D Hierarchical VO_x NRs@Si NWs Heterostructure: The Highly orientated 3 µm long Si NWs arrays were fabricated via metal-assisted chemical etching method.[13] Thereafter, VO_x NRs were grown by SPCVD on Si NWs arrays in a home-made ALD system using $VOCl_3$ and H_2O as precursors. In the SPCVD process, the as-received Si NW arrays were placed at the center of the stainless steel ALD chamber. A constant flow of 40 sccm N_2 was applied into the chamber as the carrier gas, which provided a background pressure of 4.2 Torr. The chamber temperature was kept at 650 °C. In a typical VO_x NRs growth process, $VOCl_3$ and H_2O vapor precursors were pulsed into the chamber for 1.5 and 0.75 s, respectively, and separated by purging N_2 for 60 s. Thus, one growth cycle included 0.75 s of H_2O pulsing + 60 s of N_2 purging + 1.5 s of $VOCl_3$ pulsing + 60 s of N_2 purging. After 400-cycle growth, the chamber was cooled down to room temperature naturally under N_2 flow (Scheme S1, Supporting Information).

To prepare for the electrochemical characterization, the as-received VO_x@Si heterostructure was loaded in the ALD chamber again for 100-cycle VO_x film overcoating. The growth conditions were 1 s of H_2O pulsing + 60 s of N_2 purging + 0.5 s of $VOCl_3$ pulsing + 60 s of N_2 purging at 350 °C. Fifteen samples were prepared in total. Among them, five samples were then annealed in H_2 and other five samples were annealed in O_2 at 500 °C for 8 h to engineer the chemical compositions of the VO_x NRs. Using the same deposition condition, 500-cycle ALD VO_x film was also deposited on Si NWs as a reference sample.

Structural Characterization: The morphologies of the 3D hierarchical VO_x NRs@Si NWs heterostructures were characterized by LEO 1530 GEMINI scanning electron microscopy (Zeiss, Germany). Tecnai TF-30 transmission electron microscopy (FEI, OR, USA) and X-ray diffraction (Bruker D8, Bruker, MA, USA) were implemented to study the crystal structure. X-ray photoelectron spectroscopy measurements were conducted for the elemental analysis on a Thermo Scientific K-alpha XPS system with Al Kα source.

Electrochemical Measurements: The electrochemical measurements were performed in an electrochemical cell of three-electrode systems. The VO_x NRs@Si NWs were covered by epoxy leaving an exposed active area of ≈0.5 cm^2. The reference and counter electrodes were saturated calomel electrode and Pt, respectively. 8 M LiCl solution (Sigma-Aldrich, 99.99%) was used as the electrolyte. All electrodes were connected to a potentiostat system (Metrohm Inc., Riverview, FL) for the electrochemical measurements. CV curves were measured in a suitable potential window based on the samples' characteristics with scanning rates ranging from 1 mV s^{-1} to 2 V s^{-1}. The galvanostatic C–D performances of all samples were measured under the current density varied from 0.5 to 20 A g^{-1} in their corresponding potential window. The EIS measurements were conducted by applying 10 mV alternative signals versus the open-circuit voltage in the frequency range of 100 kHz to 0. 1 Hz.

Supporting Information

Supporting Information is available from the Wiley Online Library or from the author.

Acknowledgements

This work was supported by the U.S. Department of Energy (DOE), Office of Science, Basic Energy Sciences (BES), under Award No. DE-SC0008711.

[1] M. Li, G. Sun, P. Yin, C. Ruan, K. Ai, *ACS Appl. Mater. Interfaces* **2013**, *5*, 11462.
[2] M. K. Song, S. Cheng, H. Chen, W. Qin, K. W. Nam, S. Xu, X. Q. Yang, A. Bongiorno, J. Lee, J. Bai, T. A. Tyson, J. Cho, M. Liu, *Nano Lett.* **2012**, *12*, 3483.
[3] L. Q. Mai, F. Yang, Y. L. Zhao, X. Xu, L. Xu, Y. Z. Luo, *Nat. Commun.* **2011**, *2*, 381.
[4] C. Liu, Z. Yu, D. Neff, A. Zhamu, B. Z. Jang, *Nano Lett.* **2010**, *10*, 4863.
[5] J. Zhu, L. Cao, Y. Wu, Y. Gong, Z. Liu, H. E. Hoster, Y. Zhang, S. Zhang, S. Yang, Q. Yan, P. M. Ajayan, R. Vajtai, *Nano Lett.* **2013**, *13*, 5408.
[6] J. H. Kim, K. H. Lee, L. J. Overzet, G. S. Lee, *Nano Lett.* **2011**, *11*, 2611.
[7] L. Yang, S. Cheng, Y. Ding, X. Zhu, Z. L. Wang, M. Liu, *Nano Lett.* **2011**, *12*, 321.
[8] D. Wei, M. R. Scherer, C. Bower, P. Andrew, T. Ryhanen, U. Steiner, *Nano Lett.* **2012**, *12*, 1857.
[9] J. F. Li, Y. F. Huang, Y. Ding, Z. L. Yang, S. B. Li, X. S. Zhou, F. R. Fan, W. Zhang, Z. Y. Zhou, Y. Wu de, B. Ren, Z. L. Wang, Z. Q. Tian, *Nature* **2010**, *464*, 392.
[10] J. Bae, M. K. Song, Y. J. Park, J. M. Kim, M. Liu, Z. L. Wang, *Angew Chem., Int. Ed. Engl.* **2011**, *50*, 1683.
[11] Y. Dong, G. Yu, M. C. McAlpine, W. Lu, C. M. Lieber, *Nano Lett.* **2008**, *8*, 386.
[12] W. Liang, B. D. Yuhas, P. Yang, *Nano Lett.* **2009**, *9*, 892.
[13] J. Shi, Y. Hara, C. Sun, M. A. Anderson, X. Wang, *Nano Lett.* **2011**, *11*, 3413.
[14] J. A. Shi, X. D. Wang, *Cryst. Growth Des.* **2011**, *11*, 949.
[15] M. Gnerlich, E. Pomerantseva, K. Gregorczyk, D. Ketchum, G. Rubloff, R. Ghodssi, *J. Micromech. Microeng.* **2013**, *23*, 114014.
[16] R. Warren, F. Sammoura, A. Kozinda, L. Lin, *2014 IEEE 27th Int. Conf. Micro Electro Mech. Syst.*, IEEE, Piscataway, NJ, USA, **2014**, p. 167.
[17] R. Warren, F. Sammoura, F. Tounsi, M. Sanghadasa, L. Lin, *J. Mater. Chem. A* **2015**, *3*, 15568.

[18] L. Kavan, M. Grätzel, S. E. Gilbert, C. Klemenz, H. J. Scheel, *J. Am. Chem. Soc.* **1996**, *118*, 6716.
[19] J. Shi, Z. Li, A. Kvit, S. Krylyuk, A. V. Davydov, X. Wang, *Nano Lett.* **2013**, *13*, 5727.
[20] X. Pan, G. Ren, M. N. F. Hoque, S. Bayne, K. Zhu, Z. Fan, *Adv. Mater. Interfaces* **2014**, *1*, 1400398.
[21] T. D. Manning, I. P. Parkin, *Polyhedron* **2004**, *23*, 3087.
[22] M. N. Field, I. P. Parkin, *J. Mater. Chem.* **2000**, *10*, 1863.
[23] S. D. Perera, A. D. Liyanage, N. Nijem, J. P. Ferraris, Y. J. Chabal, K. J. Balkus, *J. Power Sources* **2013**, *230*, 130.
[24] S. D. Perera, B. Patel, N. Nijem, K. Roodenko, O. Seitz, J. P. Ferraris, Y. J. Chabal, K. J. Balkus, *Adv. Energy Mater.* **2011**, *1*, 936.
[25] X. Lu, M. Yu, T. Zhai, G. Wang, S. Xie, T. Liu, C. Liang, Y. Tong, Y. Li, *Nano Lett.* **2013**, *13*, 2628.
[26] G. Wang, X. Lu, Y. Ling, T. Zhai, H. Wang, Y. Tong, Y. Li, *ACS Nano* **2012**, *6*, 10296.
[27] D. P. Dubal, D. Aradilla, G. Bidan, P. Gentile, T. J. Schubert, J. Wimberg, S. Sadki, P. Gomez-Romero, *Sci. Rep.* **2015**, *5*, 9771.
[28] Y.-T. Weng, H.-A. Pan, R.-C. Lee, T.-Y. Huang, Y. Chu, J.-F. Lee, H.-S. Sheu, N.-L. Wu, *Adv. Energy Mater.* **2015**, *5*, 1500772.
[29] J. P. Zheng, *J. Electrochem. Soc.* **1995**, *142*, 2699.
[30] K. Sun, F. H. Saadi, M. F. Lichterman, W. G. Hale, H. P. Wang, X. Zhou, N. T. Plymale, S. T. Omelchenko, J. H. He, K. M. Papadantonakis, B. S. Brunschwig, N. S. Lewis, *Proc. Natl. Acad. Sci. USA* **2015**, *112*, 3612.
[31] S. Boukhalfa, K. Evanoff, G. Yushin, *Energy Environ. Sci.* **2012**, *5*, 6872.
[32] W. F. Mak, G. Wee, V. Aravindan, N. Gupta, S. G. Mhaisalkar, S. Madhavi, *J. Electrochem. Soc.* **2012**, *159*, A1481.
[33] R. N. Reddy, R. G. Reddy, *J. Power Sources* **2006**, *156*, 700.
[34] C. K. Chan, H. Peng, G. Liu, K. McIlwrath, X. F. Zhang, R. A. Huggins, Y. Cui, *Nat. Nanotechnol.* **2008**, *3*, 31.
[35] L. Demarconnay, E. Raymundo-Piñero, F. Béguin, *J. Power Sources* **2011**, *196*, 580.
[36] S. Huang, Z. Wen, X. Zhu, Z. Gu, *Electrochem. Commun.* **2004**, *6*, 1093.
[37] S. Ji, J. Zhang, W. Wang, Y. Huang, Z. Feng, Z. Zhang, Z. Tang, *Mater. Chem. Phys.* **2010**, *123*, 510.
[38] Y. Yao, M. T. McDowell, I. Ryu, H. Wu, N. Liu, L. Hu, W. D. Nix, Y. Cui, *Nano Lett.* **2011**, *11*, 2949.
[39] J. Shi, C. Sun, M. B. Starr, X. Wang, *Nano Lett.* **2011**, *11*, 624.
[40] Z. Li, C. Yao, Y. Yu, Z. Cai, X. Wang, *Adv. Mater.* **2014**, *26*, 2262.
[41] Q. T. Qu, L. L. Liu, Y. P. Wu, R. Holze, *Electrochim. Acta* **2013**, *96*, 8.
[42] M. Beidaghi, C. Wang, *Adv. Funct. Mater.* **2012**, *22*, 4501.
[43] X. Pan, Y. Zhao, G. Ren, Z. Fan, *Chem. Commun.* **2013**, *49*, 3943.
[44] C. Hu, H. Xu, X. Liu, F. Zou, L. Qie, Y. Huang, X. Hu, *Sci. Rep.* **2015**, *5*, 16012.
[45] J.-M. Li, K.-H. Chang, C.-C. Hu, *Electrochem. Commun.* **2010**, *12*, 1800.

Received: September 14, 2016
Published online: October 14, 2016

